Bloch Skyrmions Interacting with a defect barrier

James Forsythe
Center of Emergent Materials, The Ohio State University
July 23rd, 2021

ABSTRACT

Magnetic skyrmions are vortex-like spin textures with chiral symmetry that arise within magnetic materials due to the Heisenberg exchange interaction and the Dzyaloshinskii-Moriya interaction (DMI). Due to their small size (can be less than 100 nm) and need for large magnetic fields to annihilate, they show promise as information carriers in high-density storage applications. One of these applications is for racetrack memories. To test the possibility of filtering in such applications, Bloch skyrmions were moved down a channel with a spin transfer torque towards and through a defect barrier. The width and saturation magnetization (M_s) of this barrier was varied to see if either parameter could be used as a filter for such applications. Results show that increasing the M_s of the barrier had significant effects on the size and velocity of the incident skyrmions whereas decreasing M_s did not show any significant effect. For a 20 nm barrier no permanent alterations of the skyrmion were induced, but for a 100 nm barrier of at least 5% increase in M_s there was a significant change in skyrmion behavior.

I. Background and Introduction

Skyrmions are topological spin objects that occur in magnetic systems with chiral symmetry[1]. Bloch skyrmions and Neel skyrmions are two types of skyrmions that are topologically equivalent. Bloch skyrmions occur in systems were the Dzyaloshinskii-Moriya interaction (DMI) occurs in the bulk of the materials, whereas Neel skyrmions occur in systems where the DMI is concentrated at the interface of two materials[2]. The bulk DMI that is responsible for the creation of Bloch skyrmions is due to a break in the crystal inversion symmetry and the high spin-orbit coupling (SOC) in the ferromagnetic material[3]. This can be seen in figure 1b where the bulk DMI vector is the white arrow pointing out from the sample.

The distribution of the magnetization for a Bloch skyrmion can be seen in figure 1a. The magnetization follows a vortex like pattern with radial dependence from the center of the skyrmion. This unusual property of ferromagnetic materials lies in the exchange interactions that happen within the material.

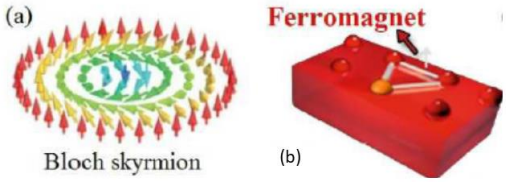

Figure. 1 (a) magnetization distribution of a Bloch skyrmions. (b) non-centrosymmetric crystal exhibiting bulk DMI vector (white arrow) due to the strong spin orbit coupling of the ferromagnetic atoms an impurity[3].

Two types of exchange interaction occurring together induce this behavior. Both of which have an associated exchange energy that must be minimized as the system tends towards its ground state. The first is the energy associated with the exchange (Heisenberg) energy which is given as

$$H_{heis} = -\sum_{i,j} J\langle \boldsymbol{S_i}|\boldsymbol{S_j}\rangle \qquad [1]$$

Where $\mathbf{S_i}$ and $\mathbf{S_j}$ are the spins of the ith and jth nearest neighbor atoms and J is the exchange constant that defines the type of interaction. To minimize the energy from this interaction the spins must be parallel or

antiparallel from one another so that the inner product of the vectors is maximized.

However, when the material has broken inversion symmetry as is the case with materials exhibiting DMI, the Heisenberg exchange interaction is not the only exchange interaction. Due to the broken inversion symmetry required for DMI to occur, the energy associated with the DMI favors orthogonal spins, which can be seen with

$$H_{DMI} = -\sum_{i,j} \boldsymbol{D_{i,j}} [\boldsymbol{S_i} \, x \, \boldsymbol{S_j}] \qquad [2]$$

Both interactions together help explain the existence of the skyrmion since it is the sum of the two that must be minimized. There are three other energies that contribute to the total energy of the system; however, these will be constant through these simulations. These energies are the Zeeman energy which is from the interaction of the system and the external magnetic field, the Demagnetizing energy which arises from long-range interactions of other magnetic moments and is characteristic of the geometry of the system, and finally the anisotropy energy which reflects the crystalline structure of the material.

The study of how skyrmions interact with defects is very important for applications since defects are pervasive in materials. Defects can be impurities that are present within the material, or they can be introduced to the material during fabrication. If an accurate understanding of the interaction of skyrmions with defects is obtained, it could be used as another mode to control skyrmions for applications. It has been found that even a single extended defect through a ferromagnetic material can create a series of attractor and saddle points depending on the driving current density[4]. Figure 2 shows a sketch of the system for this extended defect. Also, in the vicinity of certain defects, the shape of the skyrmion can deform, and if this effect increases enough, this leads to the transformation of the skyrmion into a snake-like magnetic domain[5].

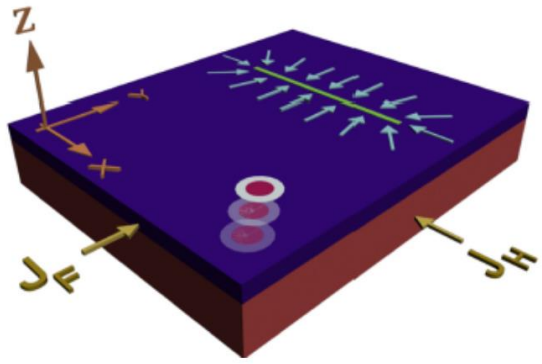

Figure 2. Sketch of the extended defect system where J_F and J_H are the current densities flowing through the ferromagnet (blue region) and the heavy metal (red region). The skyrmion is the circular red-white structure and the green line is the extended defect whose attractive force is shown as a vector-field (light-blue arrows)[4].

Skyrmions exhibit the potential to revolutionize ultra-dense magnetic memory devices and computational devices due to being exceptional information carriers. Their relevance is due to their small size, stability at room temperature in certain materials and that they can be driven by small currents[4].

Instead of the skyrmion being able to move around the extended defect through the simulations for this paper, the defect spans the entire width of the material. In this case, the skyrmion will have to penetrate the defect which is now a barrier. The behavior or the skyrmion will be simulated with different widths and saturation magnetizations of the defect.

II. Methods

The GPU-accelerated micromagnetic simulation program MuMax[3] was used to model the interaction between a Bloch skyrmion and periodic defects of varying period[6]. MuMax[3] was verified through the modelling of the magnetization angle of a

thin film problem with various saturation magnetizations while keeping the out-of-plane angle of the external field constant. MuMax[3] calculates the equilibrium point of the magnetization by discretizing the sample into small cells and numerically solving the Landau-Lifshitz-Gilbert equation in each cell through the finite element method[6].

The Landau-Lifshitz-Gilbert (LLG) equation,

$$-\frac{1}{\gamma}\frac{dM}{dt} = \left[MxH_{eff}\right] - \frac{\alpha}{\gamma M_s}\left[Mx\frac{dM}{dt}\right] \quad [3]$$

where α is the material-dependent damping coefficient, γ is the electron gyromagnetic ratio, and M_s is the saturation of magnetization. The LLG equation is used to characterize the damped precession of magnetization within magnetic matter. The second term on the right is phenomenological and acts as a restoring torque on the magnetization as the system relaxes into equilibrium. If this phenomenological term is excluded, the remaining terms describe the precession of magnetization within a ferromagnet where the left side with the time derivative of magnetization represents the torque on the system and the cross product on the right represents the Landau-Lifshitz torque that describes the precession around the effective magnetic field[4].

For the verification of MuMax[3], an infinite thin film with a non-zero magnetization is placed in an external magnetic field that is applied in the zy-plane at an angle Θ relative to the thin film surface as shown in figure 3. This problem was be reduced analytically to a transcendental function that was solved numerically. This solution was compared to the solution from MuMax[3] that was obtained by solving the LLG equation in discretized cells throughout the sample.

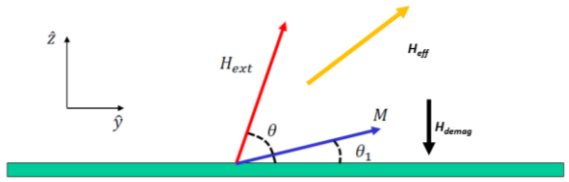

Figure 3. Visual of thin film model used for MuMax[3] verification.

How exactly the damping of the system occurs is irrelevant in finding the analytical solution for the model. This is because we are only interested in finding the ground state of the system as a function of magnetization angle and the strength of the external magnetic field, not in the dynamics in which the system undergoes to reach said ground state. Therefore, the precession of the magnetization is described by,

$$-\frac{1}{\gamma}\frac{dM}{dt} = \left[MxH_{eff}\right] \quad [4]$$

When the system is in thermodynamic equilibrium,

$$\frac{dM}{dt} = 0 \quad [5]$$

Therefore, the $\boldsymbol{M}$ and $\boldsymbol{H_{eff}}$ are parallel in the ground state of the system.

In this case, the effective field is the sum of the external magnetic field($\boldsymbol{H_{ext}}$) and the demagnetizing field($\boldsymbol{H_D}$). For thin film, the demagnetizing field is that of a uniformly magnetized ellipsoid which in general, is expressed in matrix form as

$$\boldsymbol{H_D} = -\begin{pmatrix} N_{xx} & 0 & 0 \\ 0 & N_{yy} & 0 \\ 0 & 0 & N_{zz} \end{pmatrix}\boldsymbol{M} \quad [6]$$

With the thin film infinite in the xy-plane, $N_{xx}=N_{yy}=0$ and $N_{zz}=4\pi$.

The given system and geometry lead to the demagnetizing field being

$$\boldsymbol{H_D} = -4\pi sin(\theta_1)\hat{\mathbf{k}} \quad [7]$$

where sin(Θ_1) takes the z-component of the magnetization and Θ_1 is the angle of magnetization as shown in figure 3. With the external field being,

$$\boldsymbol{H_{ext}} = H_{ext}\cos(\theta)\,\hat{\boldsymbol{j}} + H_{ext}\sin(\theta)\hat{\mathbf{k}} \quad [8]$$

where the non-bolded H_{ext} represent the magnitude of the external field. This provides us with an effective magnetic field of

$$\boldsymbol{H_{eff}} = H_{ext}\cos(\theta)\,\hat{\boldsymbol{j}} + (H_{ext}\sin(\theta) - 4\pi sin(\theta_1))\hat{\mathbf{k}} \quad [9]$$

Due to the consequence of equation [4] of the ground state of the system being when the effective field and the magnetization are parallel, the angle of magnetization for the ground state can be determined with to trigonometry of the vector components, yielding a result for the ground state angle of magnetization of

$$tan\theta_1 = \frac{H_{ext}sin\theta - 4\pi sin\theta_1}{H_{ext}cos\theta} \quad [10]$$

The above equation is shown as the analytical solution (black lines) in figure 4.

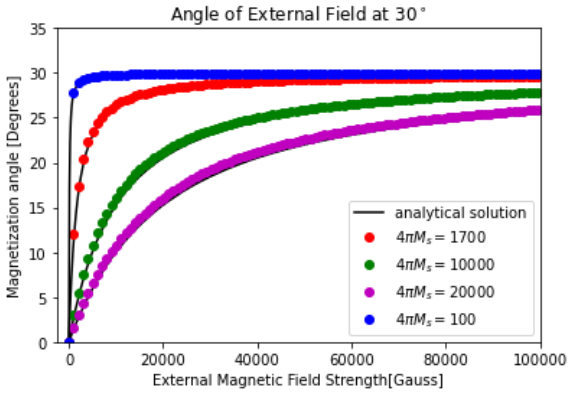

Figure 4. Numerical verification of MuMax^3 through comparing MuMax^3 calculated data with the derived analytical solution for values of $4\pi M_s$ of 100 (blue), 1700 (red), 10000 (green), 20000 (purple). No deviation from MuMax^3 acquired results and analytical solution.

Modeling skyrmions penetration through barrier in MuMax^3

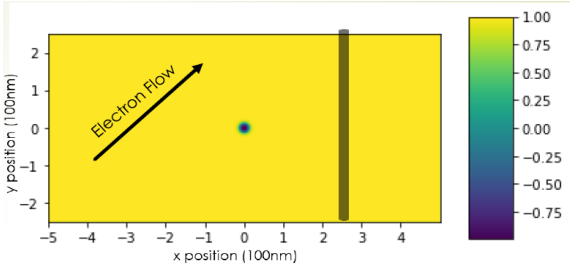

Figure 5. Schematic of model used for simulations. In this case, 20nm defect barrier is shown along with the direction of electron flow. The color scale represents the z-component of the magnetization of the respective cell.

The model used for the current simulations involved a channel that was 500nm in width and with periodic boundary conditions in the x direction. The defect started 250nm from the center of the skyrmion at the beginning of every simulation, with the width of the barriers extending in the positive x-direction away from the skyrmion. Defect barrier widths of 20 nm and 100 nm were used. The saturation magnetization (M_s) of the defect was altered from the base value of the channel, which is 437000 A/m. The M_s of the defect barrier was varied by ±1%, ±5%, and ±10%. Each of the values is given in table 1.

M_s	M_s Value [A/m]
-10%	393300
-5%	415150
-1%	432630
Base value of channel	437000
+1%	441370
+5%	458850
+10%	480700

Table 1. table of the M_s value of the corresponding percentage of the base value of the channel.

Model Parameter	Value
Exchange Stiffness	$15E^{12}$ J/m
Bulk DMI strength	$2E^{-3}$ J/m^2
Damping Constant	0.5
Uniaxial anisotropy axis	(0,0,1) (z-axis)
1st order uniaxial anisotropy constant	$0.5E^{6}$ J/m^3
Current	**($-1E^{12}$, $-1E^{12}$, 0) A/m^2**

Table 2. various parameters used to run the model along with their values.

The motion of the skyrmion was present due to the spin transfer torque from the electrons flowing at a 45^0 angle from the x-axis as shown in figure 5. This angle was chosen due to a prominent Skyrmion Hall Effect present within the material that caused the skyrmion to traverse to the side of the channel and annihilate before an adequate distance past the defect barrier was traveled.

The skyrmion behavior was observed in the model by saving the distribution of the z-component of the magnetization of each cell in the model every 0.5 ns. The skyrmion is seen as the dark blue circle in figure 5 as the z-component of the magnetization at the center is very close to -1.

III. Results and Discussion

The radius of the skyrmion as it moved through the material for the 20 nm and 100 nm barriers are shown in figure 6 and 7 respectively. As shown, the radius of the skyrmion increased or decreased depending on if the M_s of the defect barrier was greater than or less than that of the rest of the channel. As is obvious in figure 6, once the skyrmion passed through the barrier, it reverted to its original radius even when the M_s of the defect barrier had a 10% difference from the base value of the channel.

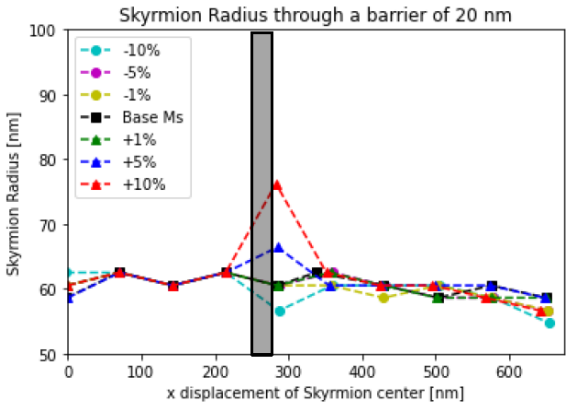

Figure 6. A graph of the radius of the skyrmion versus the displacement of the skyrmion center in the x-direction where the black box is the location of the 20 nm defect barrier.

In figure 7, the width of the defect barrier has a significant effect on the skyrmion radius as it moves throughout the channel. The width of the defect has increased to 100 nm and the skyrmion radius possess the same relationship with the M_s of the defect as it did with the 20 nm defect barrier. When the M_s of the barrier was below that of the base M_s, the radius of the skyrmion still decreased, but it remained smaller for longer as it traversed the barrier. However, when the M_s of the defect was +5% and +10% of the base M_s of the channel, the skyrmion became so large within the defect that it deformed so much that it could not revert to its original size. This deformation of the skyrmion can be seen by the progression of the +10% M_s trial in figure 13 in the appendix.

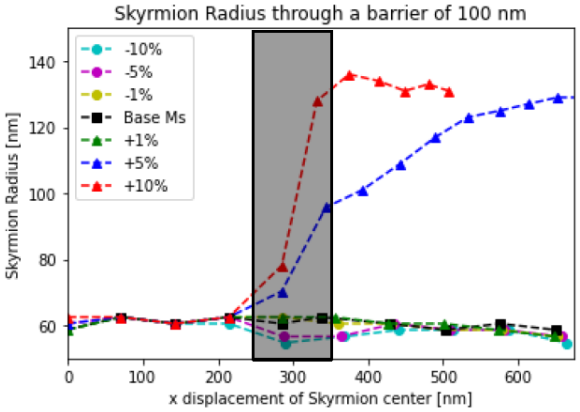

Figure 7. graph of the skyrmion radius versus the displacement of the center of the skyrmion in the x-direction where the black box is the location of the 100 nm defect barrier.

The velocity of the skyrmion was also affected by the characteristics of the defect barrier. Figure 8 shows the position of the skyrmion's center with respect to time for a defect barrier of 20 nm in width. It is shown in figure 8, that the position was a relatively straight line, with a small deviation while the skyrmion was inside of the defect barrier at 2.5 ns. This straight line shows that the skyrmion had a constant velocity in the x direction throughout its lifespan in the channel.

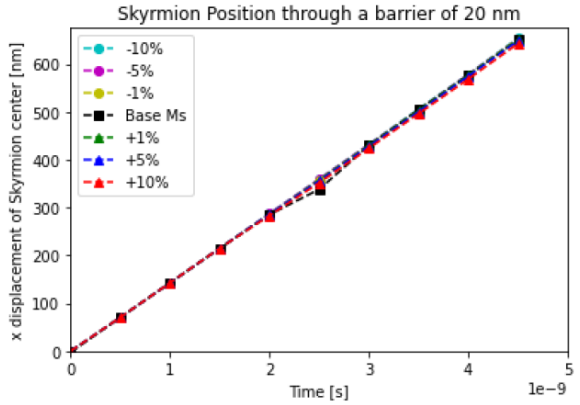

Figure 8. x-displacement of the skyrmion's center as it passed through the 20 nm barrier with respect to time.

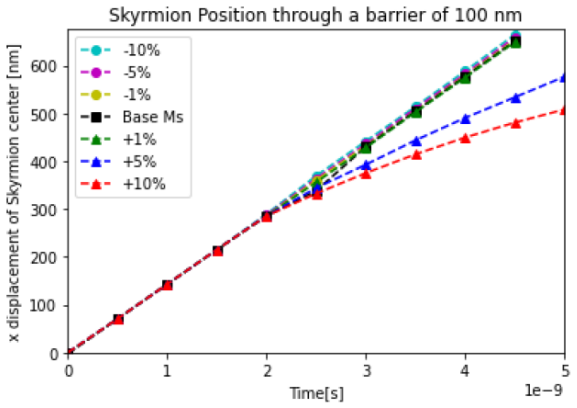

Figure 9. x-displacement of the skyrmion's center as it passed through the 100 nm defect barrier with respect to time.

When the defect barrier width increased to 100 nm, there was a noticeable change in the velocity of the skyrmions. As shown in figure 9, for -10%, -5%, -1%, and +1% M_s for the defect barrier, the exhibited behavior of the x-displacement of the skyrmion was the same for both the 20 nm and the 100 nm defect barrier. However, there is a clear divergence between the x-displacement of the center of the skyrmion of the two barrier sizes when the M_s of the defect barrier was +5% and +10% of the base value. As can be seen in figure 13 in the appendix for the case of the +10% M_s barrier, this divergence happened when the skyrmion started to increase in size due to being inside of the defect.

Figures 10 and 11 exhibit the behavior of the graphs in figures 6 through 9 in the form of the actual frames taken from the model. Each can be seen at the beginning of the appendix. Each frame is 0.5 ns in time from the initialization of the skyrmion where the black boxes are the position of the defect within the channel. The color bar in figures 10 and 11 indicate the z-component of the magnetization of each cell within the simulation, where the dark blue is inside of the wall of the skyrmion as the magnetization points downward.

IV. Conclusions

This project verified the uses of MuMax^3 for micromagnetic modeling and modeled the interactions of Bloch skyrmions with a defect barrier within a channel. It was found that when the defect barrier was of increased M_s from the base M_s of the channel, the skyrmion radius would increase while inside the barrier. Whenever the defect possessed a smaller M_s than that of the rest of the channel, the skyrmion radius would decrease while inside of the defect. In both cases, the skyrmion would revert to its original size unless it became so large inside of the barrier that it began to deform. This deformation led to the slow annihilation of the skyrmion and potential trapping of the back end of the skyrmion within the barrier. When the size of the skyrmion increased to a significant degree, the velocity of the skyrmion would decrease. If the skyrmion size did not increase too much, the velocity of the skyrmion was unaffected by the defect barrier.

V. Acknowledgments

I would like to thank Dr. Denis Pelekhov, Dr. Mohit Randeria, and Dr. P. Chris Hammel, as well as Jacob Freyermuth, Guanzhong Wu, and Matt Shmukler for their aid and advice throughout this summer research experience.

This REU program is a part of the NSF Materials Research Science and Engineering Center (MRSEC) supported under the NSF Award Number DMR-2011876.

VI. References

[1] C. H. Marrows, An Inside View of Magnetic Skyrmions *Physics* **8**, 40 (2015)

[2] X. S. Wang, H. Y. Yuan, X. R. Wang, A theory on skyrmion size and profile, *Communications Physics* **1**, 31 (2018)

[3] I. Medlej, F. El Haj Hassan, Micromagnetic modeling of skyrmion dynamics and THz oscillation in antiferromagnets. (2019)

[4] L. Gonzalez-Gomez, et al., Analytical modeling of the interaction between skyrmions and extended defects, *Physical Review B.* **100**, 054440 (2019)

[5] A. Derras-Chouk, Skyrmions Near Defects, *Journal of Physics: Condensed Matter* **33**, 195802 (2021)

[6] A. Vansteenkiste, et al. The design and verification of mumax3, *AIP Advances* **4**, 107133 (2014)

[7] G. Chen, Skyrmion Hall Effect, *Nature Phys* **13**, 112-113 (2017)

Appendix I.

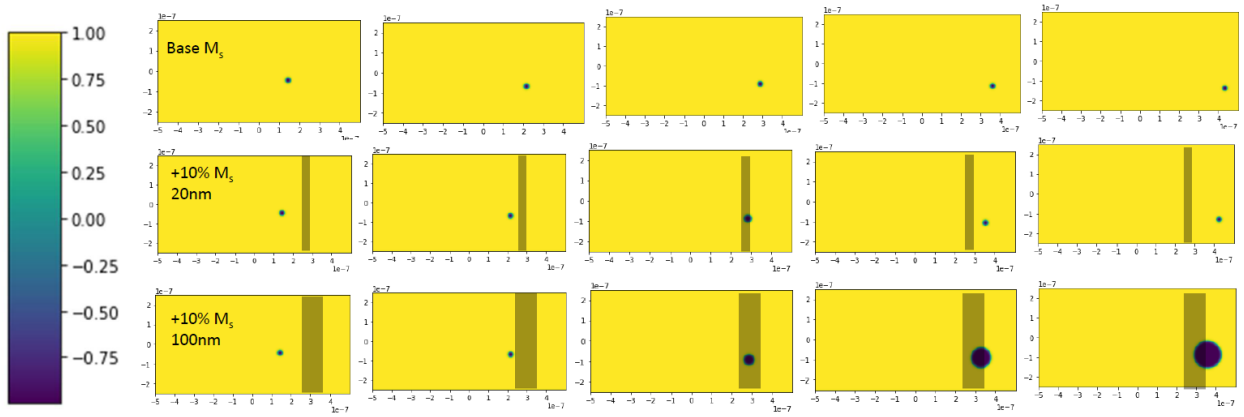

Figure 10. Comparison of the skyrmion passing through the barrier with the base M_s (top), +10% M_s in a 20nm barrier(middle), and +10% M_s in a 100nm barrier(bottom). Time in simulation is 1 ns to 3 ns.

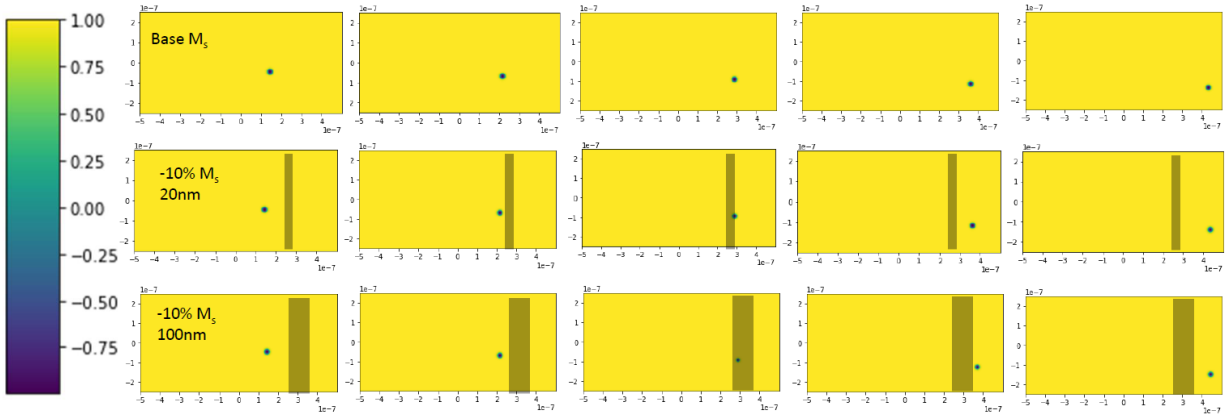

Figure 11. Comparison of the skyrmion passing through the barrier with the base M_s (top), +10% M_s in a 20nm barrier(middle), and +10% M¬s in a 100nm barrier(bottom). Time in simulation is 1 ns to 3 ns.

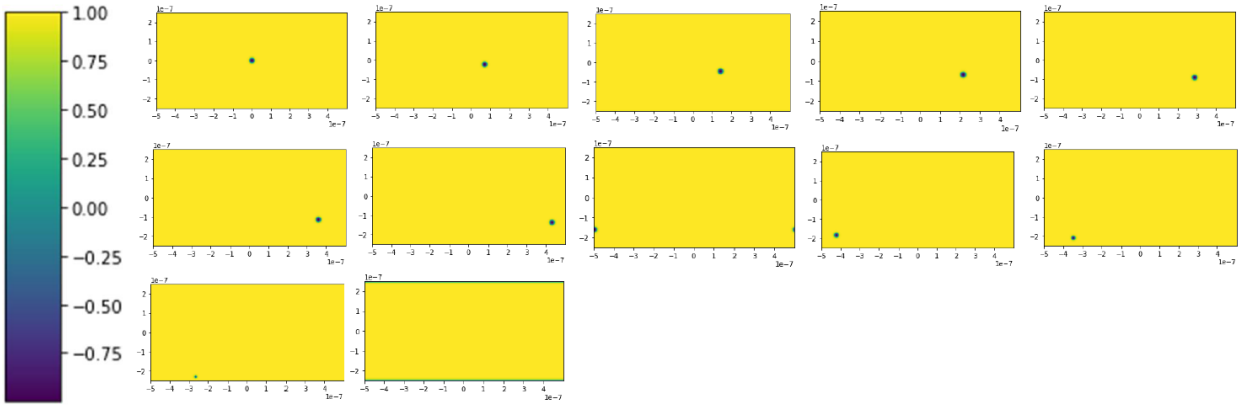

Figure 12. Full progression of skyrmion motion from initialization to annihilation for a channel without a defect (all base M_s).

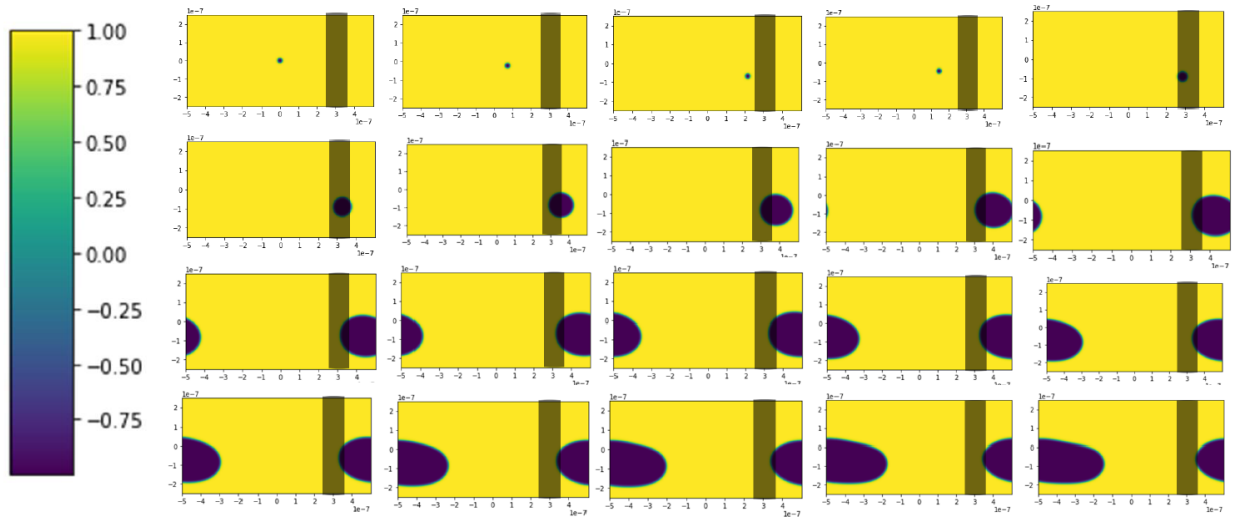

Figure 13. Full progression of skyrmion motion from initialization to annihilation for a channel with defect +10% from base M_s and 100 nm in width. .

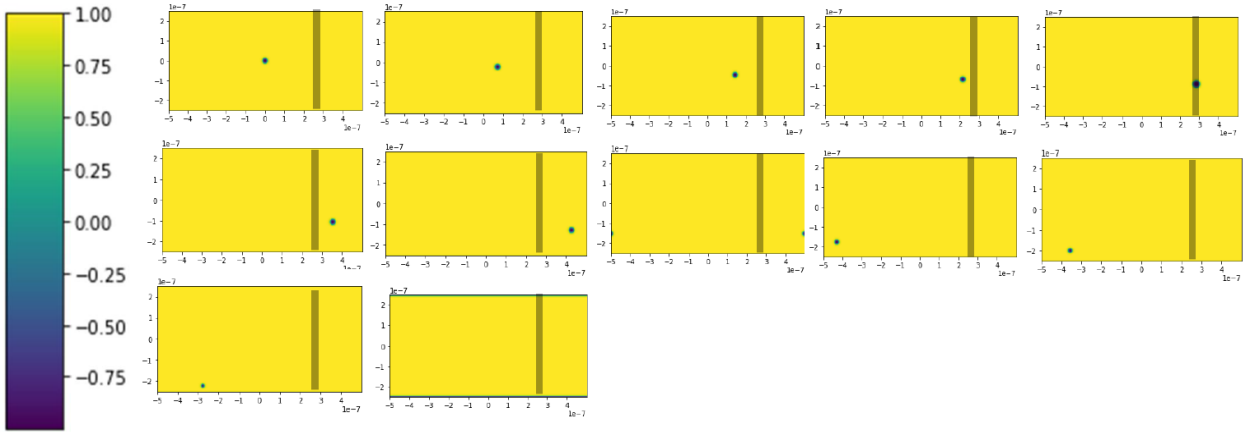

Figure 14. Full progression of skyrmion motion from initialization to annihilation for a channel with defect +10% from base M_s and 20 nm in width.

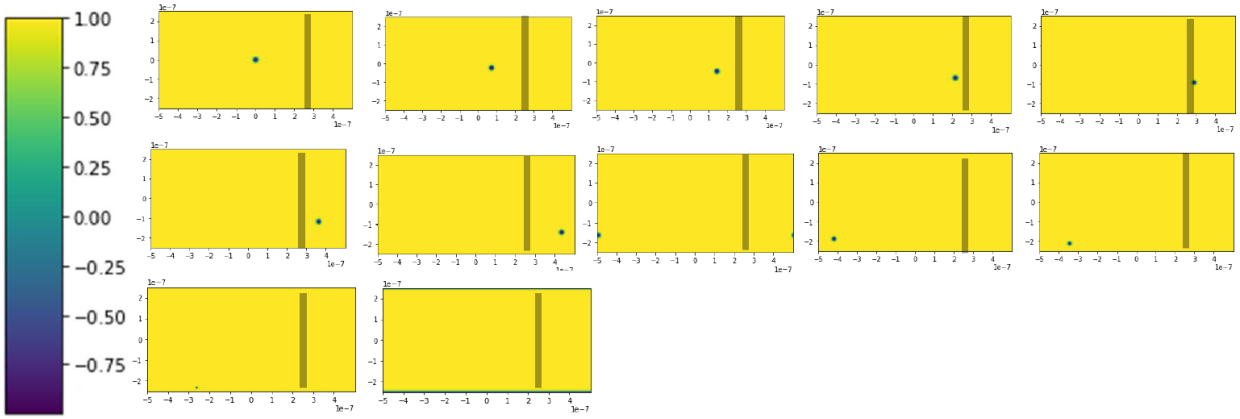

Figure 15. Full progression of skyrmion motion from initialization to annihilation for a channel with defect -10% from base M_s and 20 nm in width.

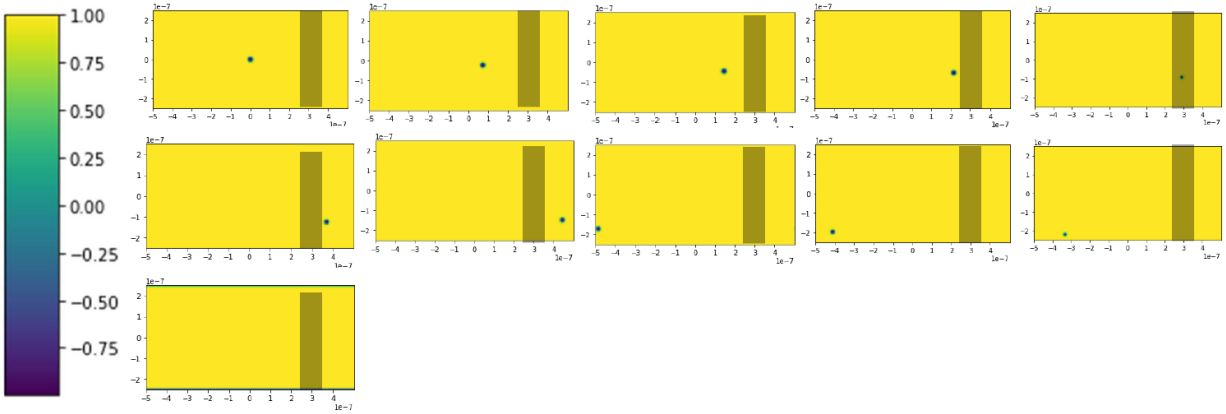

Figure 16. Full progression of skyrmion motion from initialization to annihilation for a channel with defect -10% from base M_s and 100 nm in width.